Mon. Not. R. Astron. Soc. **347,** 556–568 (2004)

Haloes around edge-on disc galaxies in the Sloan Digital Sky Survey

Stefano Zibetti,[1]★ Simon D. M. White[1] and Jon Brinkmann[2]
[1]*Max-Planck-Institut für Astrophysik, Karl-Schwarzschild-Str. 1, D-85748 Garching bei München, Germany*
[2]*Apache Point Observatory, PO Box 59, Sunspot, NM 88349, USA*

Accepted 2003 September 19. Received 2003 September 18; in original form 2003 August 28

ABSTRACT

We present a statistical analysis of halo emission for a sample of 1047 edge-on disc galaxies imaged in five bands by the Sloan Digital Sky Survey (SDSS). Stacking the homogeneously rescaled images of the galaxies, we can measure surface brightnesses as deep as $\mu_r \sim 31$ mag arcsec^{-2}. The results strongly support the almost ubiquitous presence of stellar haloes around disc galaxies, whose spatial distribution is well described by a power law $\rho \propto r^{-3}$, in a moderately flattened spheroid ($c/a \sim 0.6$). The colour estimates in g–r and r–i, although uncertain, give a clear indication for extremely red stellar populations, hinting at old ages and/or non-negligible metal enrichment. These results support the idea of haloes being assembled via early merging of satellite galaxies.

Key words: galaxies: haloes – galaxies: photometry – galaxies: spiral – galaxies: structure.

1 INTRODUCTION

The most commonly accepted paradigm for the formation of structure in the Universe, ranging from galaxies to clusters and superclusters of galaxies, predicts that they are assembled via the hierarchical clustering of dark matter (DM) haloes, in the framework of the so-called Λ cold dark matter (CDM) cosmology. Although these models have been very successful in describing large-scale structure and much recent progress has been made in understanding the processes behind the assembly of individual galaxies through numerical simulations (e.g. Navarro & White 1994; Sommer-Larsen, Gelato & Vedel 1999; Navarro & Steinmetz 2000; Scannapieco & Tissera 2003), semi-analytical modelling (e.g. Kauffmann, White & Guiderdoni 1993; Baugh, Cole & Frenk 1996; Somerville & Primack 1999), and their combination (e.g. Kauffmann, Nusser & Steinmetz 1997; Kauffmann et al. 1999; Benson et al. 2000; Springel et al. 2001), much work is still needed. The study of the stellar haloes of disc galaxies, such as our own Milky Way (MW), can give a substantial contribution in this field. From many studies (for a review see, for example, Majewski 1993), it is known that the MW halo is populated by old, metal-poor stars, whose origin is debated. They may have formed in the early stages of the dissipational collapse of the gas in the protogalactic DM halo. Alternatively they may have been accreted through the stripping of stars from satellite galaxies. Evidence that this process plays an important role in building up the stellar population of the halo has come from the Sagittarius dSph (Ibata, Gilmore & Irwin 1994), a low-latitude halo stream found in the Sloan Digital Sky Survey (SDSS; Yanny et al. 2003; Ibata et al. 2003), the ongoing disruption process of the Palomar 5 globular cluster (Odenkirchen et al. 2002), and the detection of streams in local high velocity stars (Helmi et al. 1999). How much of the halo light and mass must be ascribed to this type of interaction and how common they were in the past is still unclear.

In order to answer these questions in a more general context, the extension of the observations to a statistical sample of external galaxies is required. Unfortunately the surface brightness (SB) contributed by a stellar halo similar to that in the MW is typically 7–10 mag fainter than the central parts of the other galactic components (disc, bulge) and than the sky. At the present day, observations of the halo are available only for a handful nearby galaxies and provide varying results. Recent work by Ferguson et al. (2002) has demonstrated the presence of substructure in the moderately metal-enriched stellar halo of M31, that is likely to be the relic of the disruption of one or more small companion galaxies. The search for haloes in more distant galaxies, for which stars belonging to different components cannot be resolved, has been focused on edge-on discs, because of the much lower contamination of the halo by the projected disc stars. Problems with flat-fielding, scattered light from other background and foreground sources, and extended point spread function (PSF) wings make it extremely difficult to obtain reliable photometry down to 29–30 mag arcsec^{-2}, as required in order to characterize galactic haloes. After the first detection of a halo around NGC 5907 claimed by Sackett et al. (1994), many controversial results have followed. The latest and deepest observations of this galaxy (see, for example, Zheng et al. 1999) strongly support the extraplanar emission being instead a ring which results from tidal disruption of a satellite galaxy. In the most complete study so far, (but see Section 5 for a more exhaustive review of recent results in the literature), the deep observations of a sample of 47 edge-on galaxies, by Dalcanton & Bernstein (2002), provide evidence for the ubiquitous presence of red envelopes around disc galaxies, which the authors attribute to an old, moderately metal-enriched, thick disc structure.

★E-mail: zibetti@mpa-garching.mpg.de

© 2004 RAS

In this paper we present the results from the statistical study of halo emission from a sample of more than 1000 edge-on disc galaxies imaged by the SDSS (York et al. 2000). The SDSS is imaging about a quarter of the sky in the *u*, *g*, *r*, *i* and *z* bands, with 54-s drift scan exposures at the dedicated 2.5-m Apache Point Observatory telescope (Fukugita et al. 1996; Gunn et al. 1998; Hogg et al. 2001; Smith et al. 2002; Pier et al. 2003), reaching ∼25 mag arcsec^{-2} at a signal-to-noise (S/N) ratio of ∼1 for a single pixel. In order to reach a SB as low as 29 mag arcsec^{-2}, we adopt a stacking technique, in which we combine the images of all the galaxies. First, the images must be geometrically transformed in order to make the galaxies superposable. Other external sources must then be masked. Finally, the count statistics of each pixel is considered and a suitable estimator is chosen to represent the distribution. In this way, it is possible not only to increase the S/N ratio by a factor $\sim\sqrt{1000}$, but also to remove statistically the major sources of contamination for deep photometry of individual objects, namely foreground and background sources, inhomogeneities in the flat-field and light scattered inside the camera.

The paper is organized as follows. The sample is described in Section 2, and in Section 3 we describe the image processing and the stacking procedure. The results are analysed in Section 4, paying particular attention to the noise properties of the resulting images and to the possible sources of error and of bias. In Section 5 we give a discussion, including a comprehensive comparison with previous results in the literature and the possible implications for galaxy formation. A summary and the conclusions of this work are reported in Section 6.

2 THE SAMPLE

As of 2002 April the SDSS has covered ∼2000 deg^2 both in five-band imaging and spectroscopy. Blanton et al. (2003a) have selected a sample of galaxies from the Main Galaxy Sample (Strauss et al. 2002), also known as 'Large-Scale Structure Sample 10' (LSS10), including all sources with average SB within the Petrosian[1] radius in *r* band $\mu_r < 17.77$, that have been successfully targeted by the spectroscopic observations (see Blanton et al. 2003b, for details about the 'tiling' algorithm). We refer the reader to Blanton et al. (2003a) for the details of the sample and the regions of the sky covered.

For the purposes of this work we selected a subsample of edge-on galaxies from the LSS10 requiring the following conditions to be satisfied:

(i) Petrosian magnitude (*Pmag*) successfully measured at least in the three most sensitive SDSS passbands, namely the *g*, *r* and *i* bands;
(ii) $Pmag_i \leqslant 17.5$;
(iii) isophotal semimajor axis[2] $a > 10$ arcsec in *i* band;
(iv) isophotal axial ratio $b/a \leqslant 0.25$ in *g*, *r* and *i* bands.

Images of the 1221 selected galaxies were inspected by eye in order to prune from the sample objects that are unsuitable for stacking.

[1] Petrosian (1976) defines the Petrosian radius as the radius at which the SB equals a given fraction of the average SB inside that radius. The Petrosian flux (and hence the magnitude) is defined as the flux inside a certain number of Petrosian radii. See Stoughton et al. (2002) for the full description of the procedure adopted in the SDSS data reduction and the actual parameters.
[2] The SDSS reduction pipeline PHOTO (Lupton et al. 2001) provides an elliptical fit of the 25.0 mag arcsec^{-2} isophote parametrized by the semi-axes *a* and *b*.

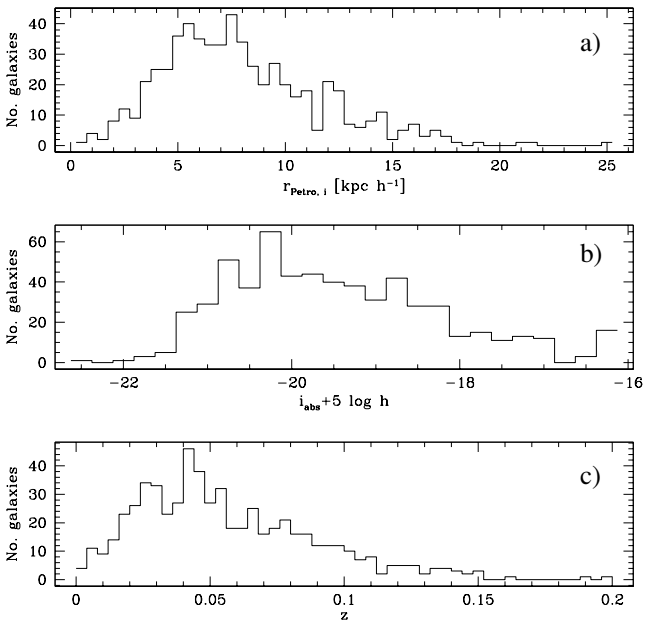

Figure 1. Distributions of the sample galaxies in Petrosian radius (panel a), absolute *i*-band magnitude (panel b), and redshift (panel c).

First of all, we discarded a few per cent of the galaxies whose axial ratios had been clearly underestimated due to some failure in the SDSS PHOTO reduction pipeline. Galaxies showing evidence of interaction with nearby companions, warps or other irregularities were rejected. The absence of nearby bright sources contaminating the background was required as well. The resulting sample is composed of 1047 galaxies, ranging from −22.5 to −16.0 *i*-band absolute Petrosian magnitude, in units of mag + 5 log *h*. The redshift distribution of the sample peaks at $z \sim 0.05$ with a standard deviation of 0.035. Typical physical dimensions range from ∼1 to ∼25 kpc h^{-1} (Petrosian radius in the *i* band), with a median value of 7.4 kpc h^{-1}. A summary of the sample properties is reported in Fig. 1. Eye inspection of the single galaxies confirms that our sample is dominated by late-type disc galaxies, with at most a few per cent of Sb-c or Sb. Most of the galaxies appear to be almost bulge-free and the remainder have quite small 'classical' bulges.

3 THE IMAGE STACKING

3.1 The image pre-processing

The raw SDSS imaging data are available as 2048 × 1489 pixel^2 (13.5 × 9.8 arcmin^2) bias subtracted and flat-fielded 'corrected frames'. Using SExtractor v2.2.2 (Bertin & Arnouts 1996) we accurately determined the centre and the position angle (PA) of the major axis for each galaxy. From the segmentation image output by SExtractor we obtain a mask for all the sources in each field detected with S/N ⩾ 1. The background level for each galaxy was determined as the mode of the pixel count distribution in an annulus with inner radius $3 \times a_{\mathrm{iso},i}$ and outer radius $6 \times a_{\mathrm{iso},i}$ (where $a_{\mathrm{iso},i}$ is the isophotal major semi-axis at 25.0 mag arcsec^{-2} in *i* band). This background was then subtracted from each image.

3.2 Photometric scalelengths

The main hypothesis underlying the stacking technique as a reliable statistical tool to investigate halo properties is an assumed

self-similarity of the disc galaxies, or at least of their diffuse component. There must exist a 'characteristic' scalelength, such that after rescaling, all galaxies can be superposed. The validity of this assumption will be discussed in more detail in Section 4.2.

Because the SB distribution of edge-on discs is affected strongly by dust extinction, we chose the i band ($\lambda_{\rm eff} = 7480$ Å) as the reference passband in order to characterize the scalelength of our sample. This choice represents the best trade-off between the need for a high sensitivity and the desire to limit the effects of dust.[3] Many different scalelengths can be defined from photometric analysis.

We consider the following four scalelengths:

(i) the Petrosian radius $r_{\rm Petro}$, as obtained from the SDSS photometric data base (see Stoughton et al. 2002; Abazajian et al. 2003);
(ii) the effective or half light radius r_{50};
(iii) the exponential scalelength $r_{\rm exp}$;
(iv) an isophotal radius obtained from the one-dimensional (1D) light profile along the major axis $r_{\rm 1D}$.

r_{50}, $r_{\rm exp}$ and $r_{\rm 1D}$ have been determined using dedicated software developed in the IRAF environment. In order to evaluate the two former parameters, we derive a SB profile from circular aperture photometry extending out to 1.5 isophotal ($\mu_i = 25$ mag arcsec^{-2}) radii. r_{50} is then obtained as the radius enclosing 50 per cent of the total flux, while the exponential scale radius $r_{\rm exp}$ is derived from the least-squares fit to the SB profile between r_{50} and r_{90} (i.e. the radius enclosing 90 per cent of the flux). The basic motivation for analysing a 1D brightness profile, derived by collapsing the image of the galaxy along the minor axis, is to have an estimate of the brightness which is as much as possible independent of the inclination. The SB enhancement is, in fact, important and severely dependent on the inclination, when the edge-on condition is approached. Assuming low or negligible extinction, the quantity

$$\zeta \equiv -2.5 \log \frac{{\rm d}Flux(x)}{x{\rm d}x},$$

where $Flux(x)$ is the flux enclosed within the projected distance x from the minor axis of the galaxy, is independent both of the inclination and of the distance of the galaxy. As a reference level for determining $r_{\rm 1D}$ we chose $\zeta = 25.0$ mag arcsec^{-2}, which corresponds roughly to a SB of $\mu = 25.0$ mag arcsec^{-2} for a typical edge-on galaxy.

All four scalelengths are quite strongly correlated, as expected for self-similar exponential profiles. The typical scatter around the 1:1 relation between pairs of corresponding scalelengths is ∼15 per cent.

3.3 The image transformation and stacking

For each of the four scalelengths considered, the median value in the sample, rounded to an integer number of pixels,[4] has been taken as reference for the rescaling, as given in Table 1. All galaxy images have been geometrically transformed using the drizzle resampling technique (as implemented in the IRAF GEOTRAN task) in order to correctly propagate the original noise properties. Each image has been translated to the galaxy centre, rotated according to the measured PA of the major axis, and expanded or contracted according to the ratio between the reference scalelength and the corresponding measured one. The same transformation has been applied to the corresponding mask, and a 'grow radius' of 10 pixels (in the original image size) around each masked pixel has been adopted in order to mask the extended PSF wings of the brightest sources. Because each image has a different photometric calibration and the measured SB of a galaxy is differently affected by Galactic attenuation, depending on its location in the sky, an intensity rescaling is needed as well. The transformation from the original pixel intensity i to the rescaled one i' is given by the following formula

$$i' = i \times 10^{-0.4(Z_{\rm p} - Z_{\rm p,ref} - K \times {\rm Airmass} - {\rm Reddening})},$$

where $Z_{\rm p}$ and $Z_{\rm p,ref}$ are the flux calibration zero-points of the image and of the reference, respectively, $K \times$ Airmass is the airmass correction, and Reddening is the attenuation due to our Galaxy, as given by Schlegel, Finkbeiner & Davis (1998). All the quantities are expressed in magnitudes.

Table 1. Median scalelengths (in arcsec) and rescaling reference values (in pixels).

$r_{\rm Petro}$		r_{50}		$r_{\rm exp}$		$r_{\rm 1D}$	
arcsec	pixel	arcsec	pixel	arcsec	pixel	arcsec	pixel
10.07	25	4.74	12	3.76	10	15.50	40

The combination of the transformed and rescaled images has been performed using the IMCOMBINE IRAF procedure. First of all, the masked pixels are rejected. The median of the count distribution of the remaining pixels is then calculated in order to obtain the median image. An average image is calculated as well, after clipping the 16 per cent percentile tails of the count distribution of the unmasked pixels. Adopting the standard approximation for the mode of a distribution

$$\text{mode} = 3 \times \text{median} - 2 \times \text{average},$$

we calculate the mode image. The resulting 512×512 pixel^2 images extend much beyond the detected emission from the galaxies and allow us to determine the properties of the background in great detail. A careful comparison between the three statistical combinations shows that, despite the conservative masking method adopted, the diffuse luminosity of sources other than the considered galaxies can result in significant skewness in the pixel count distribution and in a systematic increase of the sky SB up to 31 mag arcsec^{-2} in the i band in the outermost regions of the average frame with respect to the innermost ones, in which contaminating sources are avoided by selection. This systematic effect in the background is almost completely removed in the mode image. In the following, therefore, we will always refer to that one as the resulting stacked image.

For each stacked image, the residual background level is determined as the count mode in an annulus of 130 pixel inner radius, 96 pixel thick, and subtracted.

In Fig. 2 we present the images for the four most sensitive passbands (g, r, i, z), obtained by stacking the images rescaled according to the galaxy exponential scalelength. For the u band, the S/N is not sufficient to say anything about the presence and the characteristics of halo emission, therefore we will neglect this band in the following analysis and discussion. Rescaling according to the other scalelengths does not change the resulting images significantly, as we will demonstrate more quantitatively later on, and therefore they are not shown here. Intensity levels in Fig. 2 are coded in square-root transformation grey-scale, suitably adjusted to show the maximum extension of the low surface brightness (LSB) envelope. We superpose isophotal contours in two magnitude ranges: black contours,

[3] The z band is in fact the red-most one, but its sensitivity is about a factor of 2–3 lower than the i band.
[4] The pixel scale of the SDSS CCDs is 0.396 arcsec pixel^{-1}.

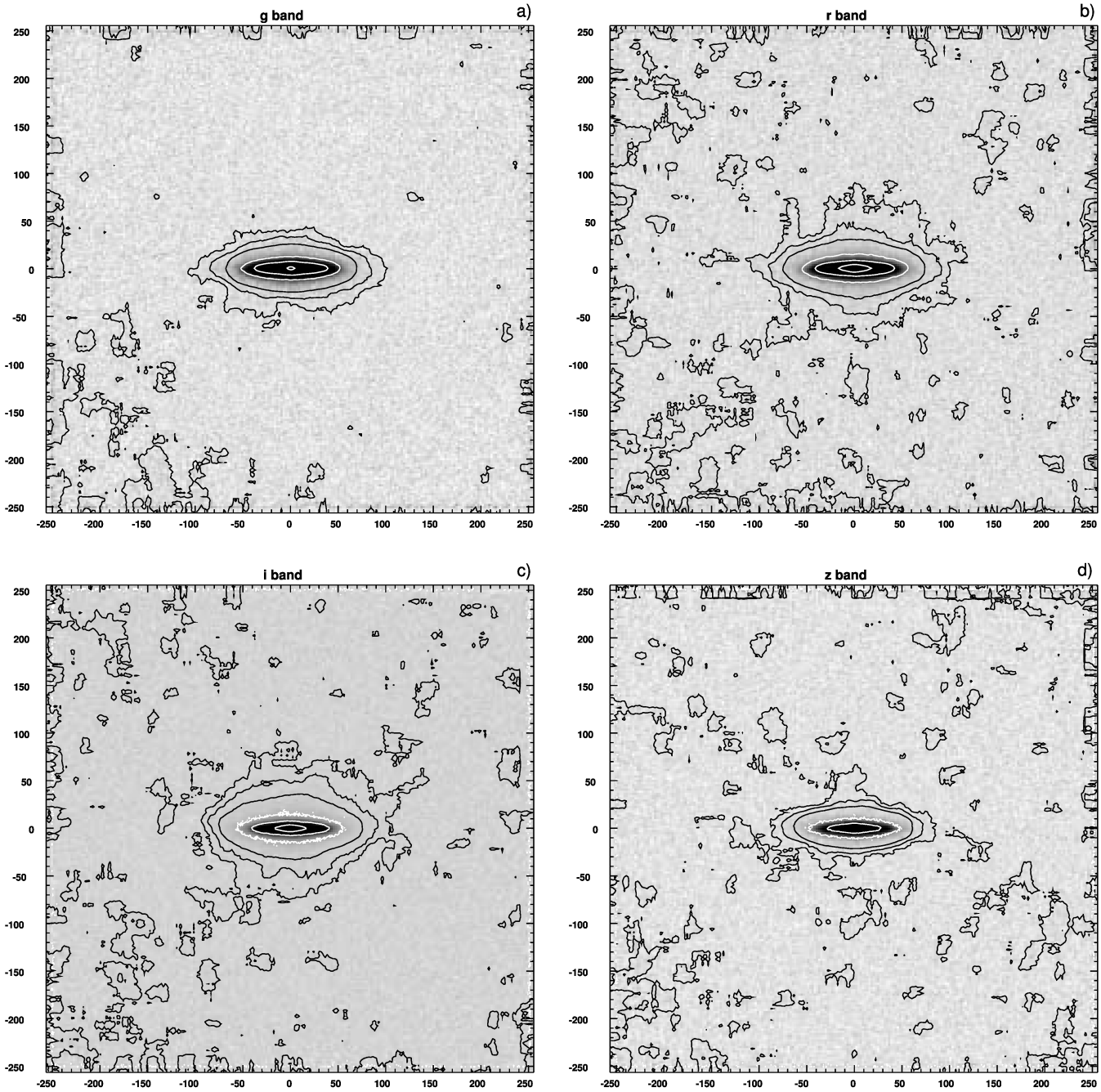

Figure 2. The images resulting from the stacking of the galaxies rescaled according to their exponential scalelength, in g, r, i and z bands. Intensity is coded in grey levels through a square-root transformation, adopting arbitrary bias and contrast. The overplotted isophotal levels are as follows: 30.0, 29.0, 28.0, 26.0, 24.0, 22.0 for the g and r bands; 29.5, 28.5, 27.5, 25.5, 23.5, 21.5 for the i band; 28.0, 27.0, 26.0, 24.0, 22.0 for the z band. See text for details. The scales indicate the offset from the galaxy centre in pixel, 10 pixels $= r_{\rm exp}$.

corresponding to the faintest isophotes, are obtained adopting a boxcar smoothing scale of 10×10 pixel^2, whereas the white, brightest ones, have been calculated with a 2×2 pixel^2 smoothing scale. The represented isophotal levels are given in the figure caption. The images and the superposed isophotes show very clearly the presence of a diffuse luminous envelope around the disc, in all four considered bands. This halo (whatever physical meaning we give to this word) is particularly evident and round in the r and i bands, whereas it is significantly flattened in the g and z bands (but the lower sensitivity in the latter band does not allow us to say much).

4 THE ANALYSIS

In this section we present the results of an analysis of the stacked images in the g, r, i and z passbands. We mainly concentrate on the stacking of the complete sample (1047 galaxies), because of the resulting higher sensitivity, but we also consider the stacking of three subsamples of bright, intermediate and low luminosity flat galaxies (Section 4.5), in order to better understand the possible dependence of the observed halo properties on total luminosity. After analysing the background properties of the stacked images in order

to assess our detection limits (Section 4.1), the photometric properties are investigated by means of radial sector-averaged SB profiles (Section 4.2), and compared to different models of luminosity distributions, namely thin+thick discs and disc+halo (Section 4.3). The average halo colours are presented in Section 4.4. Unless otherwise specified, we will always use the stacking of the images rescaled according to the exponential disc scalelength. We devote an entire paragraph in Section 4.2 to demonstrate that the adopted scalelength is not critical in determining the characteristics of the observed haloes.

4.1 The background noise properties

Because our photometric measurements are performed by integrating the flux over different image areas, as will be explained in Section 4.2, it is crucial to determine the noise properties on different scales. The presence of large-scale fluctuations is already obvious from a superficial inspection of the contour plots in Fig. 2. We restrict the analysis of the noise to the annulus (130 pixel inner radius and 96 pixel thickness) on which the sky level has been computed, and we consider the rms of the intensity after rebinning the image by different linear factors, ranging from 1 to 50. The dependence of the rms on the scalelength L is well described by a power law of the form

$$\mathrm{rms}(L) = \mathrm{rms}_0 L^{-\alpha}, \tag{1}$$

where rms_0 is the noise on one-pixel scale, and $\alpha \sim 0.7$–0.8, thus indicating that the noise has significant large-scale structure in excess to what is expected in the case of pure Gaussian noise (for which $\alpha = 1$).

4.2 The surface brightness profiles

The most obvious way to investigate the properties of the approximately round, LSB structures emerging in Fig. 2 is to extract SB profiles, averaging the flux in large wedges at different PAs. First of all, we divide the image in four circular sectors of 60° aperture, centred at 0°, 90°, 180° and 270° PAs. Each of these sectors is in turn radially divided into a number of coronae, geometrically spaced such that the outer radius of the kth corona is given by $r_k = r_0\ 1.15^k$, with $r_0 = 6$ pixels $= 0.6\ r_{\mathrm{exp}}$. Finally, we estimate the mean SB as a function of the radius for 0° (i.e. along the disc) and 90° PA (i.e. perpendicular to the disc) averaging the SB in pairs of corresponding coronae in the two symmetric sectors at 0° and 180° and at 90° and 270° PA, respectively. In each of the four graphs of Fig. 3 we show the SB profiles for the g, r, i and z images respectively, in linear scale (upper-left panel) and logarithmic scale (upper-right panel): open circles represent the 0° PA profile, filled triangles the 90° PA. The shaded areas represent the level of the rms background fluctuations at the scalelength corresponding to the area of the coronae in which the SB is averaged, as calculated in the previous section. Thus, the 1-σ detection limits for the SB profiles can be assessed as ∼31 mag arcsec^{-2} for the g, r and i bands and as ∼28 mag arcsec^{-2} for the z band.

In order to evaluate the errors on the SB we must consider contributions from (1) the background fluctuations and (2) the intrinsic scatter in the average signal from a galaxy. The first one is just provided by the background rms as evaluated in the previous section using equation (1), with L given by the square root of the area of the corona over which the signal is integrated. The estimation of the intrinsic scatter contribution is much more cumbersome, because the shape of the statistical distribution of the pixel counts in the coronae is not known a priori and the light distribution of the galaxy itself is likely to give a major contribution to the rms of the count statistics. In order to remove it, for each pixel we consider the deviation from the average intensity of the corresponding pixels in the four image quadrants, which are symmetric with respect to the x- and y-axes, and express the intrinsic rms as

$$\mathrm{rms}_{\mathrm{intrinsic}} = \sqrt{\frac{1}{3N}\sum_{i=1}^{N}\sum_{j=1}^{4}\left[I_{ij} - \langle I_{ij}\rangle_j\right]^2} \tag{2}$$

where I_{ij} is the pixel intensity, N is the number of pixels per corona per quadrant, and $\langle I_{ij}\rangle_j$ is the average intensity over the j index. In the absence of any large-scale background fluctuation, the error on the average intensity is just obtained dividing equation (2) by $\sqrt{4N}$. Adding the contribution of the large-scale fluctuations, we can write the error as

$$\sigma = \sqrt{\frac{(\mathrm{rms}(L))^2}{2} + \frac{\mathrm{rms}^2_{\mathrm{intrinsic}}}{4N}} \tag{3}$$

where rms(L) is given by equation (1) with L given by the square root of the area of the corona, and the factor 2 comes in from having averaged two coronae. Such an error estimate has been proved to be consistent with the scatter of the average intensity in the corresponding coronae in the four quadrants.

In the lower panels of each graph in Fig. 3 we plot the axial ratio b/a of the isophotes as a function of the radius (semimajor axis). This is calculated as follows. We assign a number of SB levels and determine the radius r at which such SBs are reached at different PAs θ, by interpolating the SB profiles extracted from six wedges per quadrant. Assuming $r = r(\theta)$ is well represented by an ellipse with the major axis along the x-direction, we derive the best-fitting semi-axes a and b by means of a standard least-squares algorithm.

As is apparent from the straight-line behaviour of the open circles in the linear-scale plots of Fig. 3, the profile of the wedges centred on the disc shows an exponential decrease of the SB with radius, as is typical for discs. Perpendicular to the disc, instead, the rapid initial decrease of the SB becomes shallower as we go further away from the centre of the galaxy. The trend is well approximated by a power law with index ∼2, as the straight-line behaviour of the triangles in the log-scale plots points out. This is in general true for the four bands analysed. However, the relative intensity at the same radial distance along the disc and perpendicular to it is different in different bands, reflecting a possible dependence of the flattening of the diffuse halo on the band and, in turn, this points to colour gradients in the halo itself. As already noted from the isophotal contours in Fig. 2, the halo is prominent in the r and i bands, reaching a SB comparable to that of the disc at $r \sim 8$–$10\ r_{\mathrm{exp}}$ and making the isophotal shape significantly rounder ($b/a \sim 0.5$–0.6). In the g band, the halo has very little extension (the SB drops below 31 mag arcsec^{-2} beyond $\sim 4 r_{\mathrm{exp}}$), thus leaving the isophotes extremely flattened. For the z band, the measurements are inconclusive; there is some hint of a shallowing of the slope of the profile, but the S/N drops below 1 already at ∼3 r_{exp} at the level of 28.5 mag arcsec^{-2}.

In Fig. 3, for $r > 20$ pixels, we also show as dashed lines the 'pure disc' profiles obtained subtracting the 90° profile from the 0° profile, after stretching the former by a factor of 0.6^{-1} to take the flattening of the halo into account (see Section 4.3 for details on the 0.6 factor). There is evidence that the 'pure' disc slope steepens beyond 4–5 r_{exp} in the r and i bands, consistent with studies of individual discs in the literature (see, for example, van der Kruit 2001; Kregel, van der Kruit & de Grijs 2002, and references therein), whilst the results are unclear in the g and z bands.

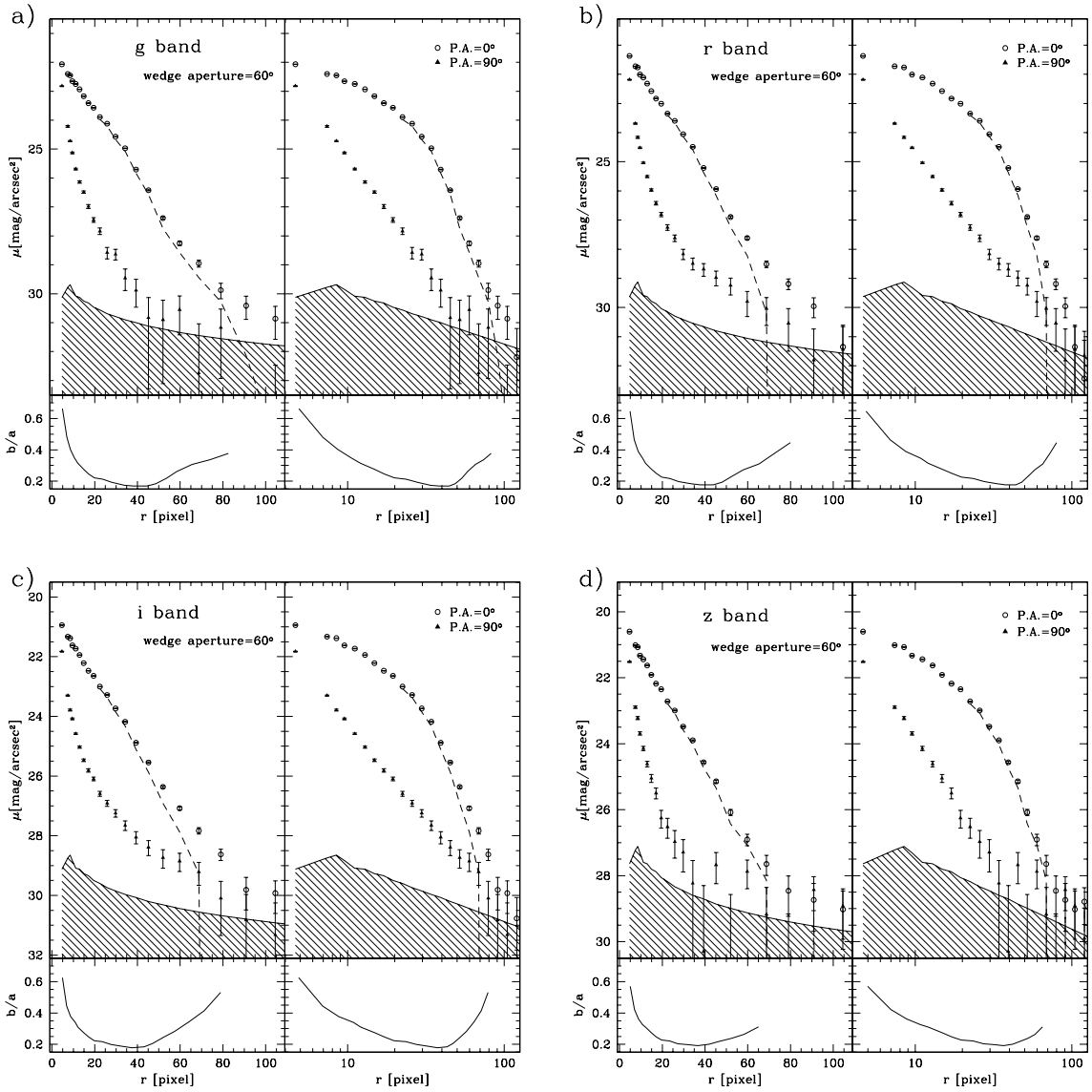

Figure 3. The SB profiles in g, r, i and z bands, in 60° wedges along the disc (PA = 0°, open circles) and perpendicular to it (PA = 90°, filled triangles). Distances from the centre in pixels (10 pixels corresponding to $1r_{\rm exp}$) are shown in linear scale (left panels) and logarithmic scale (right panels). The sky rms is represented by the shaded areas. Dashed lines represent the 'pure' disc profile at $r > 20$ pixels, obtained as explained in the text. The bottom panels of each graph show the b/a axial ratio of the isophotes as a function of the major axis a.

In order to rule out scattered light and the extended wings of the PSF as major contributors to the observed haloes, we have performed the same stacking procedure on the images of stars taken from the same frames as the galaxies to generate effective PSFs in each band. In each frame we identify a star (1) whose central brightness differs by less than 2 mag arcsec^{-2} from the central SB of the galaxy and (2) which is distant from other contaminating sources, as requested for the galaxy selection. Then, sources other than the star are masked, the frame is recentred on the star and the same geometrical transformations as applied to the galaxy are performed. The radial profile of the PSF can be reproduced by a Gaussian core plus exponential wings over a large extension. Fig. 4 shows the analytical fit to the measured PSFs in the four bands, expressed as the difference of magnitude with respect to the central SB. The decline in the core is very sharp, 6–7 mag arcsec^{-2} within five pixels, and the exponential wings contribute less than $1/10^4$ of the central SB at radii larger than 20 pixels. We will analyse the effects of the PSF on the measured profiles in the next section, by convolving with different models for the light distributions.

The characteristics of the observed halo profiles show little or no dependence on the scalelength adopted for rescaling the images of the galaxies. In Fig. 5 we plot the SB profile in the 90° PA wedge in the four bands, using different symbols for the different rescalings: open circles for $r_{\rm exp}$, filled triangles for r_{50}, open squares for $r_{\rm iso1D}$ and filled circles for $r_{\rm Petro}$. The r coordinate of each point is exactly rescaled in order to match the sample median values of the four scalelengths considered. As in Fig. 3, the shaded areas represent the sky rms. The error bars are calculated as explained before. The agreement between the different rescalings is extremely good; almost all points are consistent within the error bars, with a handful of exceptions for the $r_{\rm iso1D}$ rescaling. Even for these, the deviation is less than 3σ. Thus, we conclude that there is no systematic dependence of the average halo properties on the profile shape of the disc as described by variations in relative scalelengths.

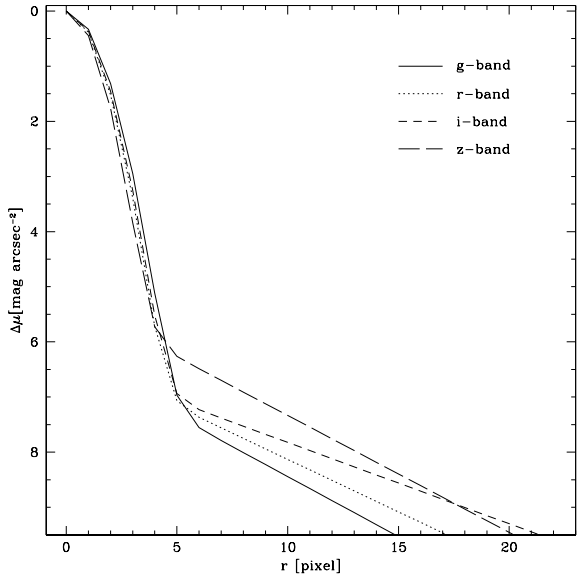

Figure 4. The PSF profiles in g (solid line), r (dotted line), i (short-dashed line) and z (long-dashed line) bands, expressed as the difference of magnitude with respect to the central SB. The lines represent the analytical fit (Gaussian core plus exponential wings) to the radial profile measured on the stacked image of stars, as explained in the text.

4.3 Modelling the halo

In this section we investigate the structural properties of the detected emission by means of simple models of the light distribution. In particular, we consider the possible contribution from a thick disc component, with an exponential vertical light density distribution, and from a (moderately) flattened power-law halo. Making predictions from models of this kind is non-trivial and must take into account that the observed emission results from a double convolution of the 'true' average light density distribution of the galaxies with (1) the distribution of inclinations and (2) the effective PSF, as computed above. The models are calculated as follows. First, we assume a particular three-dimensional distribution of light. We produce a set of 1000 Monte Carlo realizations of the projected SB, uniformly varying the inclination angle of the disc between 0 and 15 degrees (roughly corresponding to a projected axial ratio between 0 and 0.25 for an infinitely thin disc, as required by the sample selection criterion for the galaxies). The 1000 realizations are then averaged and convolved with the analytic PSF computed in the previous section, separately for each band. We do not expect to reproduce the stacked images near the nucleus nor at small distances from the disc plane, because we do not model dust extinction. Thus, we compare our models to the observations by means of vertical-cut profiles, that allow us to exclude these 'forbidden' regions. In each cut, whose width is chosen to be proportional to the distance from the minor axis of the image, we average the flux coming from the four quadrants.

In the thin+thick disc model the three-dimensional light density of each individual galaxy is assumed to be given by

$$\nu(r,z) = N \exp\left(-\frac{r}{r_{\rm exp}}\right) \times \left[\exp\left(-\frac{|z|}{z_{\rm thin}}\right) + R\frac{z_{\rm thin}}{z_{\rm thick}}\exp\left(-\frac{|z|}{z_{\rm thick}}\right)\right] \quad (4)$$

where N is the normalization factor, R is the flux ratio of the thick over the thin disc, $r_{\rm exp}$ is the exponential scalelength of the radial SB distribution, and $z_{\rm thin}$ and $z_{\rm thick}$ are the exponential vertical scalelengths of the thin and thick discs, respectively. We fix $r_{\rm exp} \equiv 10$ pixels, and $z_{\rm thin} \equiv 1$ pixel. No disc truncation is adopted. The realizations cover a logarithmic spaced grid of four by four values in the $z_{\rm thick}$–R parameter space ($z_{\rm thick}$ ranging from $10^{0.2}$ to $10^{0.8}$ pixels, R from 0.01 to 0.4). The normalization N is left as a free parameter and fitted by minimizing the χ^2. We find that the thin+thick disc models fail to reproduce the observed SB distribution of the observed haloes, because they predict a sharp exponential cut-off of the SB along the z coordinate, which is inconsistent with the observed power-law profile. In the disc+halo models, we assume a halo component with a generalized Hubble density distribution as introduced by Elson, Fall & Freeman (1987), modified to allow the iso-density surface to be oblate spheroids

$$\nu_{\rm halo}(r,z) \propto \left[1 + \frac{r^2 + (z^2/(c/a)^2)}{r_{\rm c}^2}\right]^{-(\xi+1)/2} \quad (5)$$

where c/a is the flattening parameter, $r_{\rm c}$ is the softening parameter or core radius[5] and ξ is the power-law index of the projected SB. The disc component is modelled by a double exponential distribution in r and z, without any truncation

$$\nu_{\rm disc}(r,z) \propto \exp\left(-\frac{r}{r_{\rm exp}}\right)\exp\left(-\frac{|z|}{h}\right) \quad (6)$$

with $r_{\rm exp}$ and z_0 representing the exponential scalelengths in r and z, respectively. We fix $r_{\rm c} \equiv 1$ pixel and $r_{\rm exp} \equiv 10$ pixels, and realize a grid of models in the h–ξ–(c/a) parameter space, covering the following ranges: $h = 0.50$–3.00, $c/a = 0.3$–1.0, $\xi = 1.50$–4.00. The total (disc+halo) normalization and the normalization of the halo relative to the disc for each model on the grid have been fitted by minimizing the χ^2. The best-fitting models for the g, r, i and z bands are represented in Fig. 6. For each band we plot the vertical SB profiles at four different distances $X_{\rm c}$ from the centre of the galaxy, as obtained in the vertical cuts described above, offset by 1 mag arcsec^{-2} one from the other. Even if the χ^2 are extremely high, thus demonstrating that the adopted models cannot reproduce in the details the complexity of the galaxy structure, the general agreement with the measured points is satisfactory and we are successful in reproducing the trend of the profiles. Besides the total model profiles (heavy lines), we plot also the exponential disc components alone (light lines); while dominating at small height, they give negligible contribution at $z \gtrsim 30$ pixels ($3r_{\rm exp}$). The best-fitting model parameters are reported in the panels of Fig. 6. The disc scaleheight is quite well constrained to $h \sim \frac{1}{10} r_{\rm exp}$. The power-law slope ($\xi$) is steeper in the g band (2.50), and increasingly shallower in r and i (2.00) and z (1.50) bands, while the halo shapes become increasingly rounder from $c/a = 0.50$ in g, to 0.60 in r and i, and 0.70 in the z band. This is in good agreement with the previous analysis on the images themselves and on the radial profiles. The SB of the halo component at $r = r_{\rm exp}$ along the minor axis is 25.84, 25.82, 25.03 and 25.26 mag arcsec^{-2} in the g, r, i and z bands, respectively. We can estimate the amount of halo light coming from outside the 25 mag arcsec^{-2} isophote as ∼2–3 per cent of the total galaxy light.

The models derived above allow us to quantify the pollution of the outer envelope by scattered light and PSF wings. We note that, at $r =$ 20 pixels, the PSF-convolved disc component contributes ∼30 per cent of the total SB.[6] This contribution decreases very rapidly at

[5] The core radius is introduced only for mathematical convenience, to avoid the central divergence of a pure power law.

[6] That is, 20 per cent in the g band, 33 per cent in the r and i bands and 40 per cent in the z band.

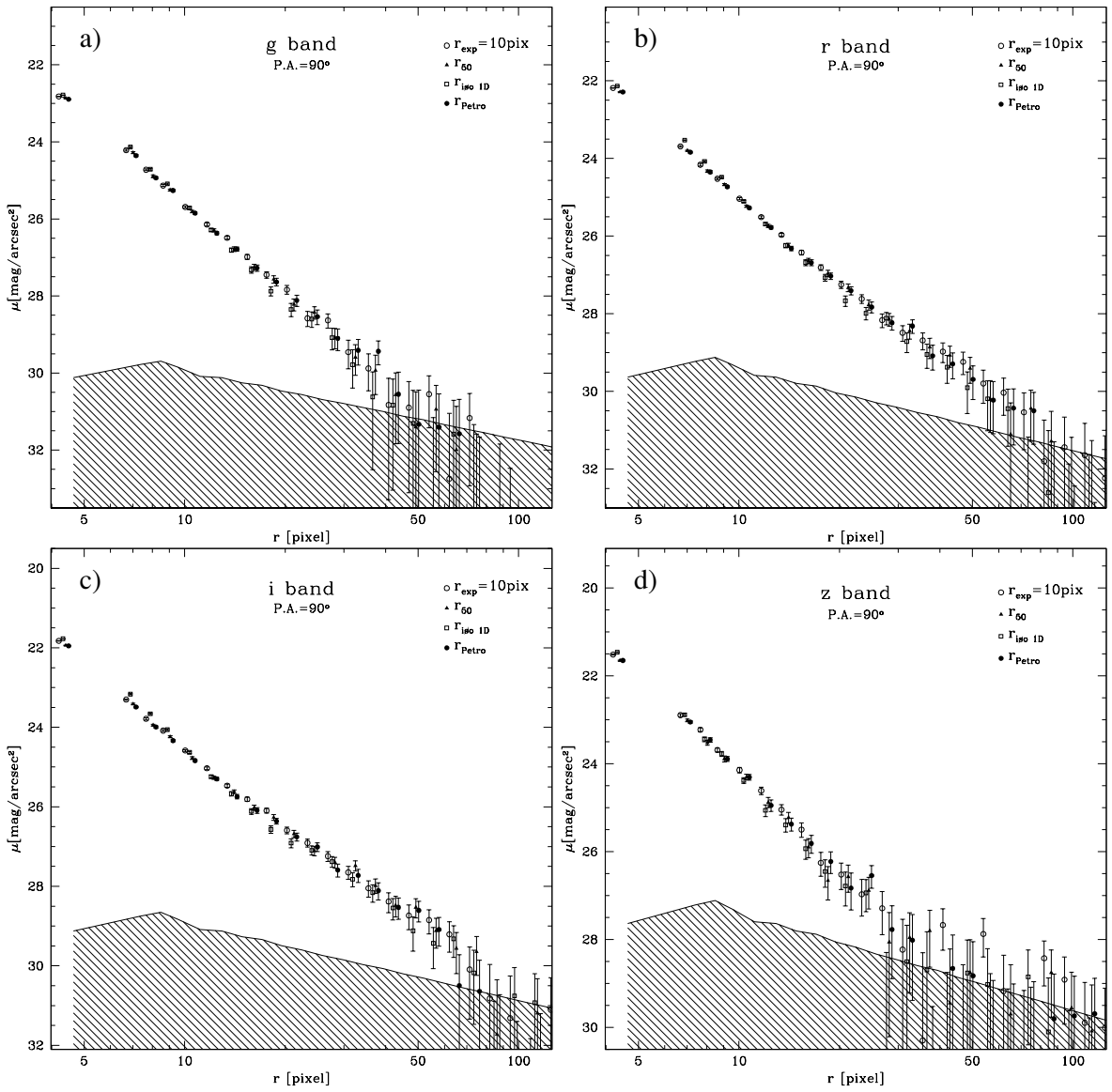

Figure 5. The SB profiles in g, r, i and z bands, at 90° PA, for different adopted rescalings. Open circles refers to images rescaled according to $r_{\rm exp}$, filled triangles to r_{50}, open squares to $r_{\rm iso1D}$ and filled circles to $r_{\rm Petro}$. The sky rms is represented by the shaded areas.

larger distances, and becomes negligible at $r > 30$ pixels in all the bands. We conclude that scattered light from the disc contributes much less than 30 per cent of the total (disc+halo) measured light beyond 20 pixels.

4.4 The halo colours

Based on the SB profiles presented in Section 4.2, we derive the colour profiles in the two 60°-aperture sectors including the disc and perpendicular to it. We concentrate on the g–r and r–i colours, excluding colours involving the z band, because of its lower sensitivity. In Fig. 7 the dots represent the colours measured perpendicular to the disc, with the error bars derived from the errors on the SB profiles; for comparison, with the dotted lines we plot the colour profiles for the disc. This has a blueing gradient toward the outer parts, which is particularly evident for g–r, but it is still clearly apparent in r–i. Disc colours (g–$r = 0.7$–0.5, r–$i = \sim 0.4$) are consistent with typical star-forming galaxies, once we allow for significant dust extinction, as expected for edge-on conditions. The increasing presence of dust near the galaxy centre and age and metallicity gradients in the disc can also easily explain the observed gradients. Beyond 4–5 $r_{\rm exp}$ there is evidence for colours becoming redder, possibly indicating that the halo is overtaking the disc. This is consistent with the steepening of the profiles of the 'pure disc', shown as dashed lines in Fig. 3.

The g–r profile perpendicular to the disc is extremely noisy; no clear trend can be established and the measurements are definitely unreliable beyond 20 pixels. The halo in these bands is roughly as red as the inner parts of the disc. The r–i colour shows instead a clear reddening toward the outskirts of the galaxy, reaching extremely red colours ∼0.8, about 0.4 mag redder than the disc. We derive the best estimate of the halo colours using the mean colour around 20 pixels and consider the uncertainties given both by the error bars and by the scatter of the points around an 'ideal', smooth profile:

$$g\text{–}r = 0.65 \pm 0.1$$

$$r\text{–}i = 0.60 \pm 0.1.$$

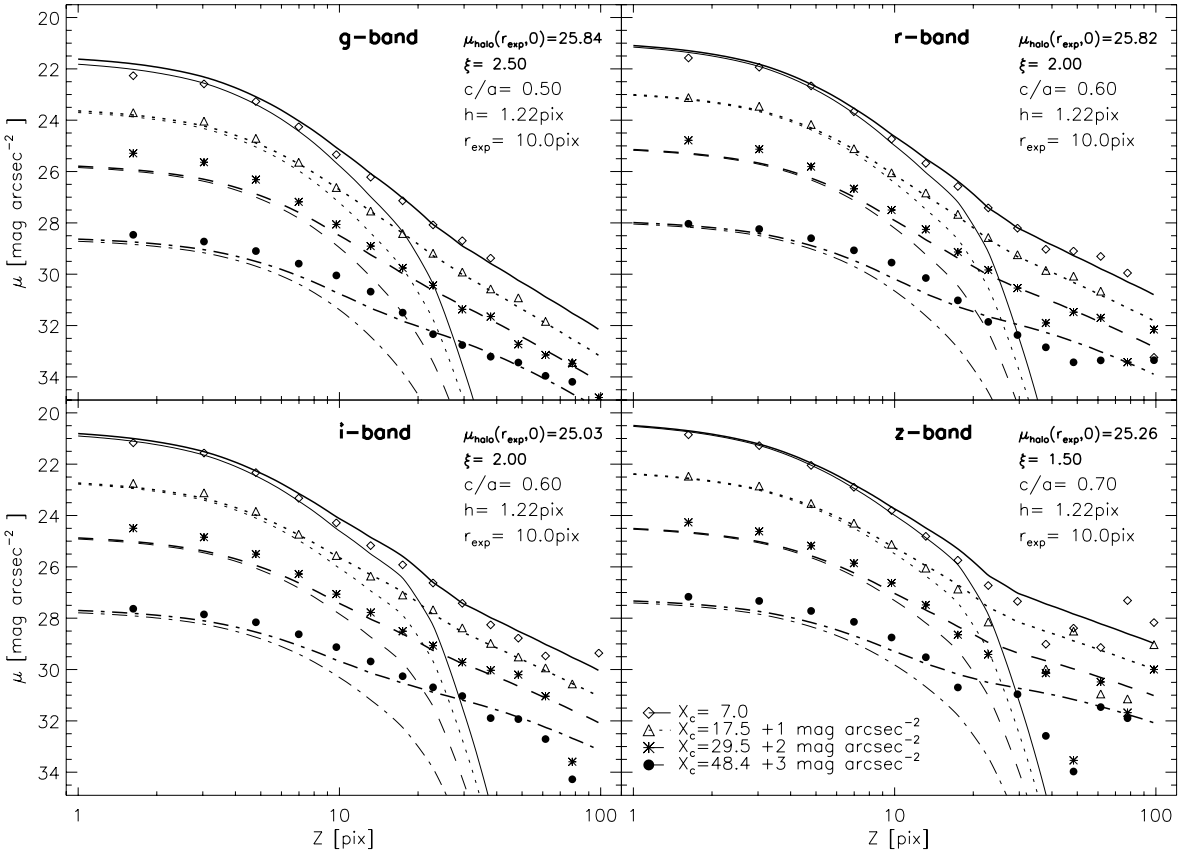

Figure 6. Vertical cut SB profiles with superposed the prediction from the power-law halo+disc model. Points are the SB measured in four vertical cuts at distance X_c from the centre (in pixel units, see legend). Profiles are offset 1 mag arcsec^{-2} from each other. Heavy lines represent the model profiles, light lines are the disc component of the model alone.

These results are not corrected for the effects of the PSF. Based on the analysis in the previous section, we estimate that the SB at $r =$ 20 pixels is polluted by scattered light from the inner parts by up to $\sim$30 per cent. However, this contribution is very similar in all the bands (20 per cent in the *g* band, 33 per cent in the *r* and *i* bands) and can redden the real halo colours by some hundredths up to 0.2 mag (worse case for *g*–*r*). It is worth stressing that this assessment has large uncertainties, due to the very simplistic nature of the models adopted here and to their extreme sensitivity to the fitting parameters (e.g. changing the vertical scalelength of the disc affects very slightly the goodness of the fit, but can significantly change the disc and scattered light contributions to the colours at 20 pixels).

The robustness and the significance of the estimates given above, will be discussed in detail in Section 5.

4.5 Dependence on the total galaxy luminosity

In order to understand the dependence of the halo features on the galaxy luminosity, we analyse the stacked images (exponential scalelength rescaling) for three luminosity bins in the *i* band, namely the 'bright' ($-22.5 < i_{\rm abs} + 5 \log h \leqslant -20.2$), the 'intermediate' ($-20.2 < i_{\rm abs} + 5 \log h \leqslant -19.0$) and the 'faint' ($-19.0 < i_{\rm abs} + 5 \log h \leqslant -16.0$). The profiles at 0° and 90° PA (obtained as in Section 4.2) are plotted in Fig. 8: open triangles for the 'faint' bin, filled squares for the 'intermediate' and open circles for the 'bright'. The solid lines running through the points are the profiles as obtained from the complete sample. We notice that the halo SB is correlated with the luminosity of the galaxy, with the less luminous ones having also fainter haloes. A similar correlation with the total luminosity holds for the disc SB as well, indicating that the relative brightness of the halo with respect to the disc is roughly constant. This luminosity dependence is barely observable in the *g* band, but becomes increasingly evident at longer wavelengths, with an average offset of $\sim$0.5 mag arcsec^{-2} between the 'bright' and the 'faint' profile in the *i* band. This also implies that the haloes of the bright galaxies are redder than the faint ones by some 0.1 mag in both *g*–*r* and *r*–*i* colours.

5 DISCUSSION

The analysis performed in the previous section provides strong evidence for the generalized presence of a diffuse, LSB stellar component around disc galaxies. By stacking more than 1000 images, we are able to extract reliable photometry at SB level as faint as $\sim$31 mag arcsec^{-2} in the *g*, *r* and *i* bands and $\sim$28 mag arcsec^{-2} in the *z* band.

It is worth stressing that the statistical estimator adopted in this work to compute the combined images is extremely robust. The evaluation of the mode for each pixel in the composite image as 3 × median −2 × average, with the average calculated over the count distribution after rejecting the 16 per cent percentile tails and the masked pixels, is effective in removing outliers and spurious contributions from other sources, and in correcting for the skewness

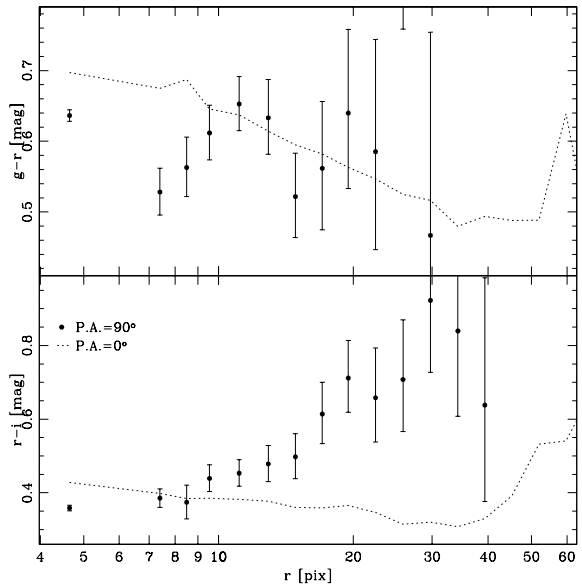

Figure 7. The g–r and r–i colour profiles. The filled circles refer to the 60°-aperture sector perpendicular to the disc, and the dotted lines represent the colours in the wedge along the disc.

of the distribution, while reducing the noise of the standard mode estimation.

The isophotal contours superposed to the images in Fig. 2 show the presence of luminous haloes whose shape is clearly rounder than the highly flattened central disc. The shape of the effective PSF, obtained from the stacking of 1000 stars selected from the same frames and with similar criteria as the galaxies, after applying the same geometrical transformations, is not consistent with scattered light and extended PSF wings giving a major contribution to the light detected in the halo. Comparisons with the light distribution expected from simple thin+thick disc models, in which we have accounted for the whole range of galaxy inclinations and for the effective PSF, demonstrate that no exponential vertical disc component can yield the observed power-law shape of the SB profiles at $r > 4\,r_{\rm exp}$ in any of the four considered bands. Adding a moderately flattened ($c/a \sim 0.6$), power-law ($I \propto r^{-2}$ or $\rho \propto r^{-3}$) halo component to a simple exponential disc, it is possible to reproduce the basic features in the observed profiles quite well.

It could be argued that the emission we detect in the outer regions is produced by small bulges. However, MacArthur, Courteau & Holtzman (2003) have shown that the bulges of disc-dominated galaxies, like those in our sample, are in general well represented by exponential laws with $h_{\rm bulge}/h_{\rm disc} = 0.13 \pm 0.06$ ($h_{\rm bulge}$ and $h_{\rm disc}$ being the exponential scalelength of the bulge and of the disc, respectively). Assuming an upper limit of $\mu_r = 18$–19 mag arcsec^{-2} for the central SB of the bulge, this implies that bulges contribute no more than 30 mag arcsec^{-2} beyond 20 pixels. The light we have measured is thus not a simple outward extension of the small bulges often seen in late-type galaxies.

We have shown in Fig. 5 that the results obtained are independent of the scalelength adopted for rescaling the galaxies; this is a strong indication for the absence of any significant dependence of halo characteristics on the detailed shape of the disc SB profile, even if it does not necessarily imply complete homology of the discs in our sample.

These results are consistent with some known features of the MW halo. Confirming previous results by Harris (1976), Zinn (1985) derived a halo stellar density declining as $r^{-3.5}$ from the distribution of the globular clusters. Similar results were obtained from the RR Lyrae distribution by Saha (1985), $\rho \propto r^{-3.5}$, by Preston, Shectman & Beers (1991), $\rho \propto r^{-3.2\pm0.1}$, and by Ivezić et al. (2000), $\rho \propto r^{-2.7\pm0.2}$. The spatial distribution of blue horizontal branch (BHB) stars (Preston et al. 1991; Kinman, Suntzeff & Kraft 1994) is in good agreement with those estimates, yielding $\rho \propto r^{-3.5}$ at height $z \gtrsim 5$ kpc $\sim 2.5\,r_{\rm exp}$ above the disc plane. The SB provided by the MW halo stars is expected to be roughly of the order of 30 mag arcsec^{-2} at $r \sim 8$ kpc $\sim 4\,r_{\rm exp}$ in the V band (Binney & Merrifield 1998, section 10.5), consistent with our measurements in the g band. The analysis by Hartwick (1987) and by Preston et al. (1991), considering RR Lyrae and BHB stars, provides an estimate for moderate flattening of the spheroidal halo $c/a \sim 0.6$, which is also consistent with the findings in this work.

Comparisons with analogous studies of external galaxies are in general difficult. Although its small distance makes M31 the easiest target for observing of the halo population of a disc galaxy, the prominence of its bulge makes it hard to disentangle the density distribution of the halo so that it is perhaps more appropriate to talk about a generic spheroid. Pritchet & van den Bergh (1994) measured the SB of M31 spheroid to $\mu_V \sim 30$ mag arcsec^{-2} and concluded that it can be modelled either by a de Vaucouleurs law or, in its outer parts, by a power law $\rho \propto r^{-5}$, which is much steeper than what we find. However, the globular cluster distribution follows $\rho \propto r^{-3}$ (Racine 1991) and there is evidence for a shallower power-law index in the outer parts of the halo from more recent observations (Irwin, private communication).

Recent observations of the red giant stars of the nearby, late-type spiral M33 (Ferguson et al., in preparation), seem to exclude the presence of a spheroidal component around this galaxy, but its nearly face-on aspect makes it difficult to draw firm conclusions.

Results from more distant galaxies are even more uncertain, because of the overwhelming difficulties in going deeper than 28 mag arcsec^{-2}. After the first claim by Sackett et al. (1994) of the detection of halo emission from NGC 5907, many discrepant measurements have been made by different groups in bands from the optical to the near-infrared (NIR; see, for example, Barnaby & Thronson 1994; Lequeux et al. 1996, 1998; Rudy et al. 1997; James & Casali 1998). The latest observations by Zheng et al. (1999) with intermediate-band filters, and by Yost et al. (2000) in optical and NIR, together with the red giant branch (RGB) star counts derived by Zepf et al. (2000) from Near-Infrared Camera and Multi-Object Spectrometer (NICMOS) observations, seem to rule out the presence of a halo, favouring instead a luminous ring produced by the tidal disruption of a dwarf companion.

However, despite the non-detection of any diffuse component in the Scd galaxy NGC 4244 by Fry et al. (1999), probably because of the low sensitivity of their observations ($\mu_R < 27.5$ mag arcsec^{-2}), many studies during the last years support the idea of a luminous envelope (thick disc or halo) surrounding many disc galaxies. Morrison et al. (1997) detected thick disc emission from NGC 891; Abe et al. (1999) have measured R and I light excesses with respect to an exponential disc model in the Scd galaxy IC 5249; Wu et al. (2002) have observed NGC 4565 at 6600 Å obtaining good accuracy photometry as faint as $\mu = 27.5$ mag arcsec^{-2} and found a halo component with power law $r^{-2.3-4.0}$. Similar results are found by Rauscher et al. (1998) in the NIR K band for ESO 240-G11 (power-law halo $\rho \propto r^{-3.5}$). After observing a sample of 47 extremely flat galaxies in B, R and K_s down to extremely faint SB, Dalcanton & Bernstein (2002) have claimed the ubiquitous presence of red stellar envelopes around disc galaxies. It is not clear

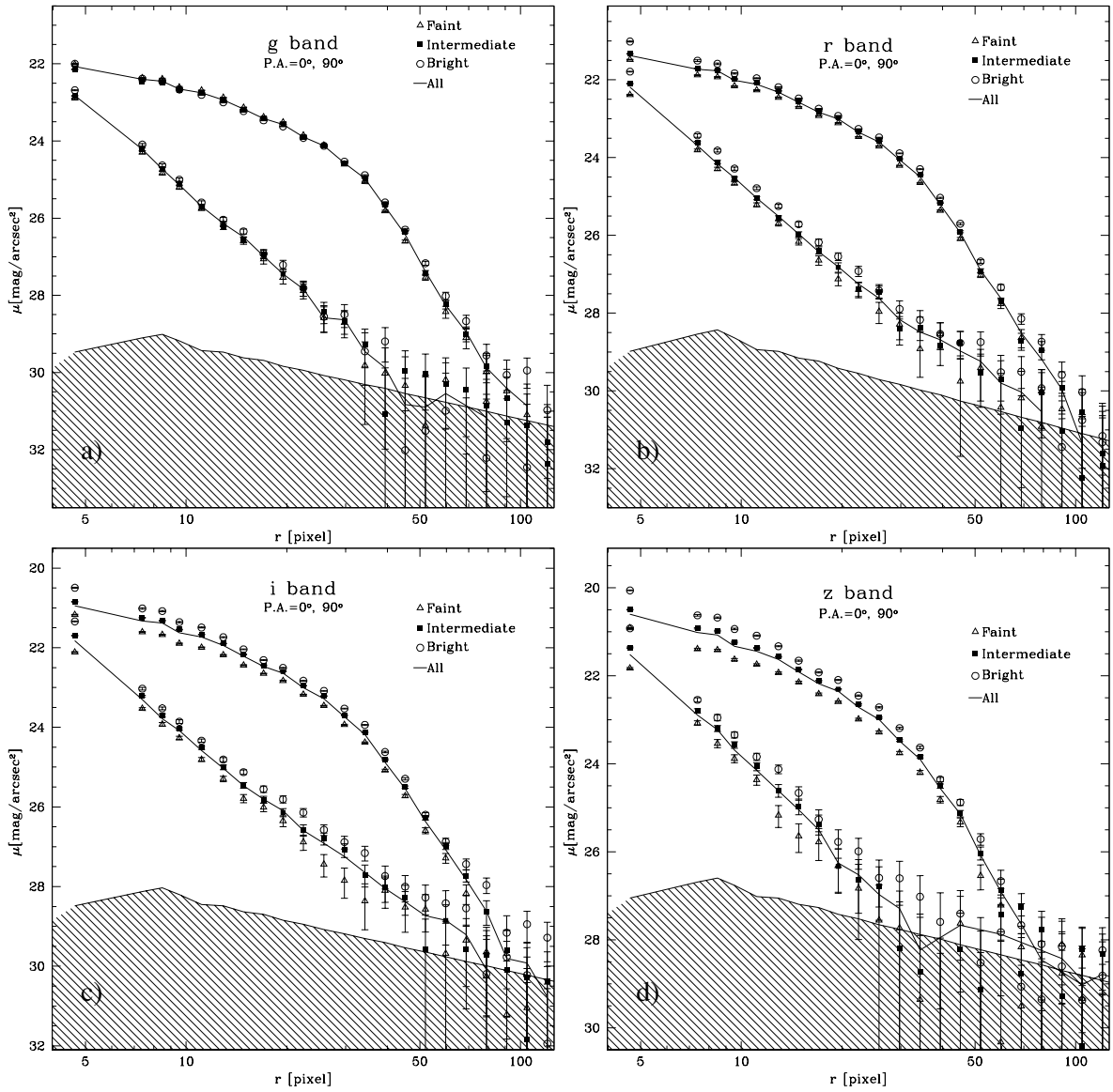

Figure 8. The stacked SB profiles in g, r, i and z bands, at 0° PA (upper curves) and 90° PA (lower curves), for three luminosity bins: open triangles represent the 'faint' bin, filled squares the 'intermediate' and open circles the 'bright' bin. The solid line is the all-sample profile. The shaded area is the rms background fluctuation.

whether these envelopes extend to a spheroidal halo or are just thick discs, as the authors claim, because their detection limits are just at the SB where we start to see our power-law halo component unambiguously.

In order to establish the origins of these stellar populations, very precise colour measurements are needed. Due to the enormous observational difficulties, reliable colour measurements of the haloes around discs are very scarce; excluding the MW, M31 and M33 for which colour–magnitude diagrams of halo stars and globular clusters can be obtained, the only optical colours available to date are those derived by Lequeux et al. (1998) for NGC 5907. Besides these, Dalcanton & Bernstein (2002) have measured (B–R) and (R–K_s) for the thick discs in their sample. The colours we derived in Section 4.4 are, in fact, very uncertain, both because of the intrinsic error of the measurements and because of the practical impossibility to avoid contributions from the disc component. The analysis in Section 4.4 showed that scattered light from the disc component is likely to affect the colours by a few hundredths of a magnitude, but colour excesses up to 0.2 mag cannot be ruled out. If we trust these results (g–$r = 0.65 \pm 0.1$, r–$i = 0.60 \pm 0.1$), we find that haloes are made of stars which are only marginally ($2\,\sigma$) consistent with old, moderately metal-poor stellar populations.

In Fig. 9 we compare the stacked halo g–r, r–i colours with different data taken from the literature.[7] Our point (open circle with error bars) is almost inconsistent with the colours of the MW globular clusters (filled circles, from Harris 1996), being much redder in r–i, and as red as the metal-rich tail of the globular cluster distribution in g–r. We have highlighted 47 Tucanae in the plot (starred dot), because its integrated colours are very similar to M31's halo. Its g–r is about the same as our measurements. We note that g–r is also

[7] Photometric transformations between different standards are taken from Smith et al. (2002).

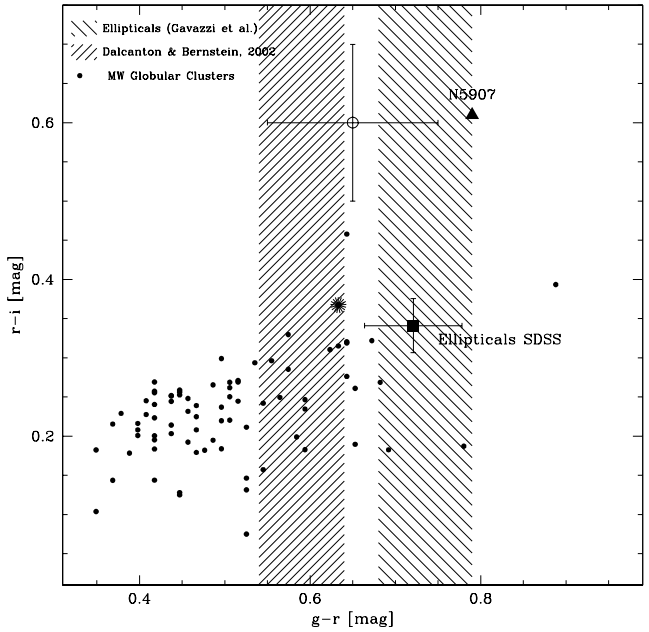

Figure 9. Comparison of the halo colours with other stellar systems in the (r–i) versus (g–r) diagram. The open circle with error bars is our measurement, filled circles are the MW globular clusters from Harris (1996), the filled square with error bar is the average±rms of the SDSS ellipticals at $z = 0.05$ from Bernardi et al. (2003), and the triangle is the measure of NGC 5907 from Lequeux et al. (1998). The shaded areas represent the g–r range for the thick discs in (Dalcanton & Bernstein (2002, /// shading) and the interquartile range of the Virgo and Coma ellipticals from GOLDMiNe (Gavazzi et al. 2003, \\\ shading).

consistent with the blue end of the elliptical sequence as derived from the SDSS at the median redshift of the sample $z = 0.05$ (filled square, Bernardi et al. 2003), and from the observations in Virgo and Coma by Gavazzi et al. in B and V, as given in GOLDMiNe (Galaxy On-Line Data base Milano Network; Gavazzi et al. 2003), whose interquartile range is represented by the back-shaded area. Reasonable agreement is found with the optical colours B–R derived by Dalcanton & Bernstein (2002) for their thick discs (whose range is represented by the shaded area in Fig. 9). Reconciling the measured r–i colour with any known stellar population is almost impossible, even if we allow for an extreme 0.1-mag reddening caused by the PSF, as discussed in Section 4.4. It is, however, interesting to note that the colours derived for NGC 5907 by Lequeux et al. (1998) are consistent with ours, but none the less troublesome. We exclude significant dust reddening for two reasons. First, the unusually red colour in our data is r–i, despite the fact that dust mostly affects optical/blue bands. Secondly, in the r–i profile there is quite strong evidence for a red gradient toward the outer parts, whereas it is known that the dust is concentrated in a thin layer in the disc. Thus, we conclude that there is evidence for the haloes being made of extremely red stellar populations. This is likely to be primarily due to an old age, but other effects, such as high metallicity or 'exotic' low-mass dominated initial mass function (IMF), would be required in order to explain the unusually high r–i.

Our red colours seem to exclude the possibility that the majority of the haloes we observe around disc galaxies are made of metal-poor stars, or that they result from the integrated light of globular cluster populations. The correlation between the disc and halo SB suggests a link between the two components. On the other hand, the high latitude extension of the emission rules out 'disc heating' as an effective formation mechanism. An accretion (or 'cannibalism') scenario, in which the halo is built up by capture and disruption of spheroidal satellites, presents many advantages in explaining the observations. In this scenario, dwarf spheroidal galaxies, made of old, metal enriched stars, are tidally disrupted by the gravitational field of the central galaxy and their stars are spread to fill the phase space almost isotropically in a few dynamical times. Thus, both the spheroidal shapes and the extremely red colours of the haloes could be explained, at least qualitatively. As already mentioned, recent observations in the halo of MW and M31, of the Sagittarius stream in the MW, and of the ring in the halo of NGC 5907 support the idea that this mechanism has been working until very recent times and is not uncommon among the disc galaxies.

Our analysis in different luminosity bins shows that the halo luminosity, at least on average, is proportional to disc luminosity. Prominent haloes are in the more luminous galaxies. The decrease of the average SB at lower luminosity affects mostly the redder passbands and is a reflection of the well-known correlation of disc SB with disc luminosity in the red bands (see, for example, Shen et al. 2003). The light we see does not appear to be a straightforward extension of the bulge, because the power-law shapes of the profiles, irrespective of luminosity, are not consistent with classical de Vaucouleurs or exponential bulges. We can interpret the halo–disc luminosity relation we find here in the hierarchical picture, in which more luminous galaxies sit in more massive DM haloes, with a larger number of merging subhaloes contributing to the stellar halo luminosity. However, deeper and more detailed observations, along with more reliable theoretical predictions for the number, stellar mass and metal content of the accreted satellites, are needed in order to confirm this hypothesis.

6 SUMMARY AND CONCLUSIONS

By stacking a large number (>1000) of edge-on disc galaxies imaged in the SDSS we have been able to detect a diffuse, spheroidal, LSB component around the disc. This detection is significant in the g, r, i and z bands, and cannot be ascribed to any obvious instrumental artefact (e.g. scattered light or PSF). Given the statistical estimator we adopt for combining the images, our result indicates that a substantial fraction of the stacked galaxies must share the observed halo characteristics, even if we cannot exclude the possibility that a number of disc galaxies actually have no halo at all. The halo can be described by a power-law projected density profile $I \propto r^{-\alpha}$, with $\alpha \sim 2$ nearly irrespective of the band.

The colour measurements provide inconclusive and troublesome results, but there is a clear indication for extremely red colours. g–r is consistent with old, moderately metal-poor stellar populations, such as the more metal-rich MW globular clusters, 47 Tucanae, the halo of M31 and the most metal-poor ellipticals. r–i is (at 2σ) 0.2 mag redder than the reddest known stellar populations in globular clusters and elliptical galaxies and it is difficult to reconcile with any theoretical models, even allowing for ad hoc modified IMFs dominated by low-mass stars and high metallicity. The data also suggest a correlation between the luminosity of the halo and the total luminosity of the galaxy.

The results presented in this work are far from being conclusive, but nevertheless they are consistent with the idea that a large fraction of disc galaxies are surrounded by a luminous halo. The colours, although affected by large uncertainties, hint at old, but not particularly metal-poor stellar populations, thus supporting a scenario in which the haloes are mostly contributed by stars stripped from

accreted or merged companions, in which the chemical evolution was already advanced.

Deeper, individual observations of a large sample of nearby galaxies will be required, however, in order to assess the validity of this scenario by quantifying not only the average halo, but also the whole distribution of individual halo parameters.

ACKNOWLEDGMENTS

We wish to thank the referees James Lequeux and Francoise Combes for helpful advice.

SZ wishes to thank Annette Ferguson, Stéphane Charlot, Amina Helmi and Tim McKay for useful discussions.

Funding for the creation and distribution of the SDSS Archive has been provided by the Alfred P. Sloan Foundation, the Participating Institutions, the National Aeronautics and Space Administration, the National Science Foundation, the US Department of Energy, the Japanese Monbukagakusho, and the Max Planck Society. The SDSS Web site is http://www.sdss.org/.

The SDSS is managed by the Astrophysical Research Consortium (ARC) for the participating institutions. the participating institutions are the University of Chicago, Fermilab, the Institute for Advanced Study, the Japan Participation Group, Johns Hopkins University, Los Alamos National Laboratory, the Max-Planck-Institute for Astronomy (MPIA), the Max-Planck-Institute for Astrophysics (MPA), New Mexico State University, University of Pittsburgh, Princeton University, the United States Naval Observatory, and the University of Washington.

REFERENCES

Abazajian K. et al., 2003, AJ, 126, 2081
Abe F. et al., 1999, AJ, 118, 261
Barnaby D., Thronson H. A., 1994, AJ, 107, 1717
Baugh C. M., Cole S., Frenk C. S., 1996, MNRAS, 283, 1361
Benson A. J., Baugh C. M., Cole S., Frenk C. S., Lacey C. G., 2000, MNRAS, 316, 107
Bernardi M. et al., 2003, AJ, 125, 1882
Bertin E., Arnouts S., 1996, A&AS, 117, 393
Binney J., Merrifield M., 1998, Galactic Astronomy. Princeton University Press, Princeton, NJ
Blanton M. R. et al., 2003a, ApJ, 592, 819
Blanton M. R., Lin H., Lupton R. H., Maley F. M., Young N., Zehavi I., Loveday J., 2003b, AJ, 125, 2276
Dalcanton J. J., Bernstein R. A., 2002, AJ, 124, 1328
Elson R. A. W., Fall S. M., Freeman K. C., 1987, ApJ, 323, 54
Ferguson A. M. N., Irwin M. J., Ibata R. A., Lewis G. F., Tanvir N. R., 2002, AJ, 124, 1452
Fry A. M., Morrison H. L., Harding P., Boroson T. A., 1999, AJ, 118, 1209
Fukugita M., Ichikawa T., Gunn J. E., Doi M., Shimasaku K., Schneider D. P., 1996, AJ, 111, 1748
Gavazzi G., Boselli A., Donati A., Franzetti P., Scodeggio M., 2003, A&A, 400, 451
Gunn J. E. et al., 1998, AJ, 116, 3040
Harris W. E., 1976, AJ, 81, 1095
Harris W. E., 1996, AJ, 112, 1487
Hartwick F. D. A., 1987, in NATO ASIC Proc. 207, The Galaxy. The structure of the Galactic halo. Reidel, Dordrecht, pp. 281–290
Helmi A., White S. D. M., de Zeeuw P. T., Zhao H., 1999, Nat, 402, 53
Hogg D. W., Finkbeiner D. P., Schlegel D. J., Gunn J. E., 2001, AJ, 122, 2129
Ibata R. A., Gilmore G., Irwin M. J., 1994, Nat, 370, 194
Ibata R. A., Irwin M. J., Lewis G. F., Ferguson A. M. N., Tanvir N., 2003, MNRAS, 340, L21
Ivezić Ž. et al., 2000, AJ, 120, 963
James P. A., Casali M. M., 1998, MNRAS, 301, 280
Kauffmann G., White S. D. M., Guiderdoni B., 1993, MNRAS, 264, 201
Kauffmann G., Nusser A., Steinmetz M., 1997, MNRAS, 286, 795
Kauffmann G., Colberg J. M., Diaferio A., White S. D. M., 1999, MNRAS, 303, 188
Kinman T. D., Suntzeff N. B., Kraft R. P., 1994, AJ, 108, 1722
Kregel M., van der Kruit P. C., de Grijs R., 2002, MNRAS, 334, 646
Lequeux J., Fort B., Dantel-Fort M., Cuillandre J.-C., Mellier Y., 1996, A&A, 312, L1
Lequeux J., Combes F., Dantel-Fort M., Cuillandre J.-C., Fort B., Mellier Y., 1998, A&A, 334, L9
Lupton R. H., Gunn J. E., Ivezić Z., Knapp G. R., Kent S., Yasuda N., 2001, in ASP Conf. Ser. 238, Astronomical Data Analysis Software and Systems X. The SDSS Imaging Pipelines. Astron. Soc. Pac., San Francisco, p. 269
MacArthur L. A., Courteau S., Holtzman J. A., 2003, ApJ, 582, 689
Majewski S. R., 1993, ARA&A, 31, 575
Morrison H. L., Miller E. D., Harding P., Stinebring D. R., Boroson T. A., 1997, AJ, 113, 2061
Navarro J. F., Steinmetz M., 2000, ApJ, 538, 477
Navarro J. F., White S. D. M., 1994, MNRAS, 267, 401
Odenkirchen M., Grebel E. K., Dehnen W., Rix H., Cudworth K. M., 2002, AJ, 124, 1497
Petrosian V., 1976, ApJ, 209, L1
Pier J. R., Munn J. A., Hindsley R. B., Hennessy G. S., Kent S. M., Lupton R. H., Ivezić Ž., 2003, AJ, 125, 1559
Preston G. W., Shectman S. A., Beers T. C., 1991, ApJ, 375, 121
Pritchet C. J., van den Bergh S., 1994, AJ, 107, 1730
Racine R., 1991, AJ, 101, 865
Rauscher B. J., Lloyd J. P., Barnaby D., Harper D. A., Hereld M., Loewenstein R. F., Severson S. A., Mrozek F., 1998, ApJ, 506, 116
Rudy R. J., Woodward C. E., Hodge T., Fairfield S. W., Harker D. E., 1997, Nat, 387, 159
Sackett P. D., Morrison H. L., Harding P., Boroson T. A., 1994, Nat, 370, 441
Saha A., 1985, ApJ, 289, 310
Scannapieco C., Tissera P. B., 2003, MNRAS, 338, 880
Schlegel D. J., Finkbeiner D. P., Davis M., 1998, ApJ, 500, 525
Shen S., Mo H. J., White S. D. M., Blanton M. R., Kauffmann G., Voges W., Brinkmann J., Csabai I., 2003, MNRAS, 343, 978
Smith J. A. et al., 2002, AJ, 123, 2121
Somerville R. S., Primack J. R., 1999, MNRAS, 310, 1087
Sommer-Larsen J., Gelato S., Vedel H., 1999, ApJ, 519, 501
Springel V., White S. D. M., Tormen G., Kauffmann G., 2001, MNRAS, 328, 726
Stoughton C. et al., 2002, AJ, 123, 485
Strauss M. A. et al., 2002, AJ, 124, 1810
van der Kruit P. C., 2001, in ASP Conf. Ser. 230, Galaxy Discs and Disk Galaxies Truncations in Stellar Disks. Astron. Soc. Pac., San Francisco, pp. 119–126
Wu H. et al., 2002, AJ, 123, 1364
Yanny B. et al., 2003, ApJ, 588, 824
York D. G. et al., 2000, AJ, 120, 1579
Yost S. A., Bock J. J., Kawada M., Lange A. E., Matsumoto T., Uemizu K., Watabe T., Wada T., 2000, ApJ, 535, 644
Zepf S. E., Liu M. C., Marleau F. R., Sackett P. D., Graham J. R., 2000, AJ, 119, 1701
Zheng Z. et al., 1999, AJ, 117, 2757
Zinn R., 1985, ApJ, 293, 424

This paper has been typeset from a TEX/LATEX file prepared by the author.